



Full Text View

[Volume 29, Issue 2 \(February 1999\)](#)

Journal of Physical Oceanography

Article: pp. 119–144 | [Abstract](#) | [PDF \(1.23M\)](#)

Dynamics of Separating Western Boundary Currents

Ibson C. A. da Silva*

Ocean Process Analysis Laboratory, Institute for the Study of Earth, Oceans and Space, University of New Hampshire, Durham, New Hampshire

Glenn R. Flierl

Department of Earth, Atmospheric and Planetary Sciences, Massachusetts Institute of Technology, Cambridge, Massachusetts

Wendell S. Brown

Ocean Process Analysis Laboratory, Institute for the Study of Earth, Oceans and Space, University of New Hampshire, Durham, New Hampshire

(Manuscript received June 4, 1996, in final form February 12, 1998)

DOI: 10.1175/1520-0485(1999)029<0119:DOSWBC>2.0.CO;2

ABSTRACT

In this work, Pratt and Stern's quasigeostrophic, $1\frac{1}{2}$ -layer, infinite jet model is connected to a western boundary by a system of two converging boundary currents. The model has a piecewise constant potential vorticity structure and the departing jet has a zonal cusplike profile in the ocean interior. The relative strengths of the coastal jets can be varied and the coastline can be tilted relative to north. The coastline tilt and the coastal current asymmetry cause an alongshore momentum imbalance that creates a spatially damped, quasi-stationary wave pattern. The presence of the boundary favors the long waves in the model, which behave fairly linearly in all study cases. The effects of the coastline tilt and the coastal current asymmetry are varied to reinforce or cancel each other. In the former case, a retroflection type of boundary current separation, like the one observed in most Southern Hemisphere western boundary currents, is obtained. In the latter case, a much smoother separation results, as when the Gulf Stream leaves the North American coast. In order to comply with the piecewise constant potential vorticity constraint, the β effect is included in the model only very crudely. The "beta" term in the potential vorticity relationship is totally compensated for by a steady flow pattern similar to the edge between two Fofonoff gyres. It is found that when β is nonzero, the wavelengths are somewhat shorter than those of f -plane cases.

Table of Contents:

- [Introduction](#)
- [The model formulation](#)
- [Numerical experiments](#)
- [Applications](#)
- [Summary and conclusions](#)
- [REFERENCES](#)
- [APPENDIX](#)
- [TABLES](#)
- [FIGURES](#)

Options:

- [Create Reference](#)
- [Email this Article](#)
- [Add to MyArchive](#)
- [Search AMS Glossary](#)

Search CrossRef for:



- [Articles Citing This Article](#)

Search Google Scholar for:

- [Ibson C. A. da Silva](#)

1. Introduction

- [Glenn R. Flierl](#)
- [Wendell S. Brown](#)



Meanders and Rossby-wave-like motion are often found in regions where western boundary currents separate from continental margins. In some cases, the current separation is smooth and the meander amplitudes increase toward the ocean interior ([Fig. 1a](#) ). In others, the current overshoots its separation latitude and retroflects (i.e., turns back on itself), forming a large amplitude lobe near the coast and meanders that decay in the downstream direction ([Fig. 1b](#) ). Eddy detachment may occur in both types of separation. When the separation is smooth, eddies are pinched off in the downstream region, where the western current extension may be regarded as a free jet. When a current retroflects, the eddy shedding usually takes place close to the coast.

[Ou and De Ruijter \(1986\)](#) reproduced both types of boundary current separation using a steady, semigeostrophic equivalent-barotropic model that employed only current inertia and the variation of the Coriolis parameter in a constant potential vorticity field. The transport magnitude dictated the separation latitude of the jets. The coastline angle (relative to north) dictated the type of separation. Obtuse angles led to retroflexion, while more acute angles produced smooth separation and long standing-wave patterns in the ocean interior.

Ou and De Ruijter's theoretical results are verified in [Campos and Olson's \(1991\)](#) summary of types of western boundary current separation. Looking at the major midlatitude western boundary currents, the latter authors attribute the smooth separation of the Gulf Stream and the Kuroshio to the fact that both North American and Japanese coasts are tilted toward the east of their general northward direction, following the current. By contrast, all the Southern Hemisphere boundary currents (i.e., the Brazil, East Australia, and Agulhas Currents) that separate from coasts tilted toward the west (of their general southward direction) tend to retroflect.

In the present work, we investigate theoretically the wave motion and meandering associated with separating western boundary currents. Unlike [Ou and De Ruijter's \(1986\)](#) work, we include time variability and make potential vorticity nonconstant in order to account for the contrast between the boundary current water and its surroundings. We employ a "contour dynamics" approach to the problem [the reader is referred to [Pullin \(1992\)](#) for a review on the contour dynamics method]. There are several examples in the literature where contour dynamics has been successfully used to investigate geophysical flows, particularly jet and vortex dynamics. [Stern and Pratt \(1985\)](#) studied barotropic shear flows. [Pratt and Stern \(1986\)](#), hereafter referred to as PS86) examined eddy detachment in infinite equivalent-barotropic jets. [Stern and Flierl \(1987\)](#) modeled interactions between vortices and jets. [Polvani et al. \(1989\)](#) investigated vortex dynamics in a two-layer fluid. [Meacham \(1991\)](#) examined meander development in barotropically and baroclinically unstable jets.

The model used in this work is based on PS86's jet model and has the following principal characteristics:

- Boundary current separation due to a convergence (or collision) of two coastal currents at some separation latitude ([Fig. 2](#) ). This approach was originally used by [Cessi \(1991\)](#) on a viscous system, and by [Agra and Nof \(1993\)](#) on an inviscid system. As an example, the Gulf Stream separation near Cape Hatteras may be interpreted as the convergence of its warm waters with the weaker southward flow of colder slope water. The Brazil Current retroflects as the region of the confluence between the Brazil and the Malvinas Currents at about 38°S.
- The coastal current convergence forming a zonal jet downstream. The axis of the major boundary current extension (such as the Gulf Stream extension and the South Atlantic Current) is oriented mainly east–west, having motivated most theoretical models of infinite jets in the literature.
- Inertial equivalent-barotropic physics in a fully nonlinear quasi-geostrophic system. The equivalent-barotropic (or 1½-layer) approximation, where a finite upper layer overlies an infinitely deep motionless layer, is the simplest mathematical formulation for simulating the highly baroclinic structure of the western boundary currents.
- A piecewise constant quasigeostrophic potential vorticity field, as required by the contour dynamics technique. Low uniform potential vorticity is mostly associated with the northward boundary current and high potential vorticity with the opposing, southward-flowing current region ([Fig. 2](#) ). Thus, away from the coast, the zonal jet has uniform cyclonic (positive) potential vorticity on one side of the discontinuity and anticyclonic (negative) potential vorticity on the other side as in PS86. This structure is intended to mimic the meeting of warmer (low potential vorticity) and often stronger boundary currents with colder (higher potential vorticity) and weaker flows in the opposite direction.
- An asymmetry in the transport of the converging currents in the model, prescribed by setting different potential vorticity magnitudes in each half of the model's domain.
- A straight coastline, which can be tilted relative to north–south. It separates land from an infinitely deep ocean.

Campos and Olson (1991, Fig. 1) indicates that the continental shelf break for four out of the five midlatitude basins can be reasonably approximated as a tilted straight line (the exception is the Agulhas Current).

- Incorporation of the beta effect, but only very crudely. To comply with the piecewise constant potential vorticity constraint, a time-independent flow field, which resembles the edge between two Fofonoff gyres, is included in the model to compensate for the β term. This introduces a westward tendency but does not allow Rossby waves.

We intend to examine the dynamical roles of coastline angle, transport asymmetry, and the beta effect, as boundary currents separate from the coast according to the simple geometry sketched in Fig. 2.

The mathematical formulation of the model is detailed in section 2. The results of the time-dependent model experiments are reported in section 3. The model is applied to the Gulf Stream, Brazil Current, and North Brazil Current in section 4. A summary of our main findings is presented in section 5.

2. The model formulation

The flow in a contour dynamics model is governed by conservation of the quasigeostrophic potential vorticity q . Since q is taken to be piecewise constant, all the action in this model is confined to the discontinuity (i.e., a contour). The contour is a material line that separates two pools of uniform potential vorticity with opposite signs (Fig. 2). If the equivalent-barotropic potential vorticity equation is nondimensionalized, using the scales of Table 1, it takes the form

$$\frac{d}{dt}q = \left[\frac{\partial}{\partial t} - \frac{\partial\psi}{\partial y} \frac{\partial}{\partial x} + \frac{\partial\psi}{\partial x} \frac{\partial}{\partial y} \right] q = 0, \quad (1)$$

where

$$q = (\nabla^2 - 1)\psi + \beta y_e, \quad (2)$$

ψ is the quasigeostrophic streamfunction, β is the Rossby parameter, and y_e is the northward coordinate. Equation (2), known as the inversion relationship, relates the flow structure to the potential vorticity field.

The model frame of reference has been rotated anticlockwise by an angle θ from the usual “earth” Cartesian coordinate system (x_e, y_e) to make the y axis parallel to the western boundary (Fig. 2). Hence the x and y directions in the model correspond to the cross-shore and alongshore directions, respectively. The angle θ can also be regarded as the prescribed angle that assures the outflowing jet is zonal ($y_e = \text{const}$) at $x_e = \infty$.

In subsection 2a, we formulate the model for the case in which q has a “symmetric” potential vorticity distribution (same magnitude but opposite sign in each half of the model). In subsection 2b, we describe the model for an asymmetric potential vorticity configuration.

a. The symmetric front model

The symmetric model represents two converging boundary currents that have the same transport and thus contribute equally in forming the zonal inertial jet. The nondimensionalized q is equal to -1 in the lower half of the model and $+1$ in the upper half. The potential vorticity front is connected to the coast (Fig. 3a). The inversion relationship [Eq. (2)] for this case may be rewritten as

$$(\nabla^2 - 1)\psi + \beta y_e = -1 + 2\mathcal{H}(y - \bar{y}(x) - \eta(x, t)), \quad (3)$$

where

$$\bar{y}(x) = -x \tan\theta \quad (4)$$


is the “undisturbed” latitude of the zonal jet as x_e approaches ∞ expressed in terms of the model coordinates, $\eta(x, t)$ is the time-dependent deviation relative to $\bar{y}(x)$, and

$$\mathcal{H}(y) = \begin{cases} 0 & \text{for } y < 0 \\ 1 & \text{for } y > 0, \end{cases}$$

represents the Heaviside step function. The two nondimensional parameters of the symmetric model [Eq. (3)] are β and θ . Since we assume that the planetary vorticity gradient is much smaller than the relative vorticity, β is kept small throughout the experiments using the symmetric model, with $\beta = 0.1$ being the maximum value considered. This assumption is consistent with the fact that we intend to investigate primarily the separation of midlatitude boundary currents, for which β is small compared to the shear within the currents. Regarding θ , we will limit our study to the two cases in which the western boundary is either oriented north–south ($\theta = 0$) or tilted at $\theta = \pi/4$.

Following [Stern and Flierl \(1987\)](#), we take advantage of the linear nature of [Eq. \(3\)](#) and subdivide the streamfunction in three parts; namely,

$$\psi = \psi_0 + \beta\psi_\beta + \psi_1. \quad (5)$$

The ψ_0 component, associated with the undisturbed (or straight and zonal) position of the front ([Fig. 3b](#) ) is defined by

$$(\nabla^2 - 1)\psi_0 = q_0 = -1 + 2\mathcal{H}(y - \bar{y}(x)). \quad (6)$$

The ψ_β component, associated with the flow due to the beta effect in a piecewise constant potential vorticity field, is defined by

$$(\nabla^2 - 1)\psi_\beta = -y_e. \quad (7)$$

The ψ_1 component, associated with disturbances or the time-dependent deviations from the undisturbed position of the front, is given by

$$\begin{aligned} (\nabla^2 - 1)\psi_1 = q_1 = & 2[\mathcal{H}(y - \bar{y}(x) - \eta(x, t)) \\ & - \mathcal{H}(y - \bar{y}(x))]. \end{aligned} \quad (8)$$

All three fields satisfy the boundary condition $\psi = 0$ at the coast ($x = 0$).

The partition of ψ is done mainly for computational (operational) reasons, as we shall see later. The reader should be aware that “undisturbed” and “disturbed” fields, in our cases, do not correspond to the conventional meanings of “mean” or “perturbed” fields, respectively. Therefore, the $\psi_0 + \beta\psi_\beta$ field does not (necessarily) represent a steady solution to the problem defined here.

The four boundary conditions needed to solve for ψ_0 are that of zero normal flow at the coast,

$$\psi_0 = 0 \quad \text{at } x = 0; \quad (9a)$$

the two conditions establishing the symmetry of the two converging coastal currents,

$$\psi_0 = -(1 - e^{-x}) \quad \text{as } y \rightarrow \infty \quad (9b)$$

and

$$\psi_0 = (1 - e^{-x}) \quad \text{as } y \rightarrow -\infty; \quad (9c)$$

and the condition that assures that the separating jet has a cusplike profile in the ocean interior,

$$\psi_0 = \text{sgn}(-y_e)(1 - e^{-|y_e|}) \quad \text{as } x_e \rightarrow \infty. \quad (9d)$$

Given θ , the ψ_0 fields are determined numerically by iteration using [Eqs. \(6\)](#) and [\(9\)](#). [Figure 4](#) shows the respective ψ_0 fields for the two different coastline orientations considered.

The ψ_β component is determined analytically. To solve for ψ_β , we impose $u_\beta \rightarrow -1$ as $x_e \rightarrow \infty$ and $\psi_\beta = 0$ at the center of the zonal jet. The choice of $\psi_\beta = 0$ at $y_e = 0$ is arbitrary, meant to match the latitude of the ψ_0 centerjet streamline and oppose the convergence of the coastal currents in the ψ_0 field. Hence, the solution is, simply,

$$\psi_\beta = x \sin\theta + y \cos\theta(1 - e^{-x}), \quad (10)$$

which is shown for $\theta = 0$ and $\pi/4$ in [Fig. 5](#).

Given the solution for the time-independent part of ψ , why is it that $\psi_0 + \beta\psi_\beta$ may not represent a steady-state solution to the problem? In a steady-state system, q contours coincide with streamlines (or vice versa). Consider the $\theta = 0$ case ([Fig. 4a](#)); the streamline $\psi_0 = 0$ coincides with the contour \bar{y} . The beta streamline $\psi_\beta = 0$ is also a straight line along $y = y_e = 0$. Therefore, in this case the $\psi_0 + \beta\psi_\beta$ solution does represent a steady state. The same is not true for the $\theta = \pi/4$ case ([Fig. 4b](#)), in which there is a clear mismatch between the straight contour \bar{y} and the $\psi_0 = 0$ streamline (which is curved) near the coast, as enlarged in [Fig. 4c](#). The $\psi_\beta = 0$ streamline is also curved.

The ψ_1 field is computed by integrating [Eq. \(8\)](#) using the Green's function method,

$$\begin{aligned} \psi_1 &= \iint G(x, y|x', y') q_1 dx' dy' \\ &= -2 \iint_D G(x, y|x', y') dx' dy', \quad (11) \end{aligned}$$

where D is the area between the curves

$$y = \bar{y}(x) + \eta(x, t) \quad \text{and} \quad y = \bar{y}(x),$$

as indicated in [Fig. 3c](#) by the alternate dark-shaded and unshaded areas.

According to PS86, the Green's function takes the form:

$$G = G_+ + G_- = -\frac{1}{2\pi} K_0(r_+) + \frac{1}{2\pi} K_0(r_-), \quad (12)$$

where K_0 is the modified Bessel function of the second kind of order zero, G_- represents the image point required to satisfy $\psi_1 = 0$ at the western boundary, and

$$\begin{aligned} r_+^2 &= (x - x')^2 + (y - y')^2, \\ r_-^2 &= (x + x')^2 + (y - y')^2. \end{aligned}$$

The disturbed velocity field is determined from [Eq. \(11\)](#), according to streamfunction definition,

$$(u_1, v_1) = \left(-\frac{\partial}{\partial y}, \frac{\partial}{\partial x} \right) \psi_1, \quad (13)$$

and using [Eqs. \(11\)](#) and [\(12\)](#).

The contour dynamics technique requires [Eq. \(13\)](#) be written in terms of contour integrals. According to PS86, we need to express the x and y derivatives in terms of x' and y' . We then follow [Wang's \(1992\)](#) derivation in using the symmetry properties of the Green's function to write

$$\frac{\partial}{\partial x} G_+ = -\frac{\partial}{\partial x'} G_+ \quad (14a)$$

$$\frac{\partial}{\partial x} G_- = \frac{\partial}{\partial x'} G_- \quad (14b)$$

$$\frac{\partial}{\partial y} G_+ = -\frac{\partial}{\partial y'} G_+ \quad (14c)$$

$$\frac{\partial}{\partial y} G_- = -\frac{\partial}{\partial y'} G_- \quad (14d)$$


For example, the disturbed alongshore velocity v_1 becomes

$$v_1 = 2 \int \int_D \left[\frac{\partial}{\partial x'} G_+ - \frac{\partial}{\partial x'} G_- \right] dx' dy',$$

where we have combined [Eqs. \(13\)](#) and (14).

We then invoke the divergence theorem,


$$\begin{aligned} v_1 &= 2 \int \int_D \nabla \cdot (G_+ \mathbf{i}' - G_- \mathbf{i}') dx' dy' \\ &= 2 \int_{\partial D} (G_+ - G_-)(\mathbf{i}' \cdot \mathbf{n}') dl' \\ &= -2 \int_{\partial D} (G_+ - G_-) dy', \end{aligned}$$

where ∂D is the contour enclosing D (the arrows in [Fig. 3c](#)  indicate the direction of the integration), \mathbf{n}' is the unit vector normal to ∂D , dl' is the infinitesimal increment along ∂D , and \mathbf{i}' is the unit vector in the x' direction.

An analogous procedure can be applied to obtain the disturbed cross-shore velocity u_1 in terms of contour integrals. Using the Green's function definitions [\[Eq. \(12\)\]](#) in the velocity expressions yields

$$u_1 = \frac{1}{\pi} \int_{\partial D} [K_0(r_+) - K_0(r_-)] dx' \quad (15a)$$

$$v_1 = \frac{1}{\pi} \int_{\partial D} [K_0(r_+) + K_0(r_-)] dy'. \quad (15b)$$

Partitioning the streamfunction field was chosen so that [Eqs. \(11\)](#) and (15) do not involve improper integrals, which potentially behave poorly (PS86). Rather, ∂D in Eq. (15) has finite boundaries (see [Fig. 3c](#) ) .

However, Eq. (15) still has a logarithmic singularity because $K_0(r) \simeq -\ln(r)$ when r is very small. The singularity is circumvented following [Polvani \(1988\)](#) through a simple integration by parts of Eq. (15), leading to the nonsingular expressions

$$u_1 = \frac{1}{\pi} \left[\int_{\partial D} (x - x') K_1(r_+) \frac{dr_+^2}{2r_+} + \int_{\partial D} (x + x') K_1(r_-) \frac{dr_-^2}{2r_-} \right] \quad (16a)$$





$$v_1 = \frac{1}{\pi} \left[\int_{\partial D} (y - y') K_1(r_+) \frac{dr_+^2}{2r_+} + \int_{\partial D} (y - y') K_1(r_-) \frac{dr_-^2}{2r_-} \right], \quad (16b)$$

where K_1 is the modified Bessel function of the second kind of order one.


Finally, how does the potential vorticity front evolve? Material particles along the q front (or the contour) are moved by the total velocity, which in our case is a combination of the undisturbed, beta, and disturbed flow fields, according to

$$\begin{aligned} \frac{d}{dt} x &= u \\ &= u_0(x, \bar{y} + \eta) + \beta u_\beta(x, \bar{y} + \eta) \\ &\quad + u_1(x, \bar{y} + \eta, t) \end{aligned} \quad (17a)$$

$$\begin{aligned} \frac{d}{dt} (\bar{y} + \eta) &= v \\ &= v_0(x, \bar{y} + \eta) + \beta v_\beta(x, \bar{y} + \eta) \\ &\quad + v_1(x, \bar{y} + \eta, t). \end{aligned} \quad (17b)$$

The (u_0, v_0) and (u_β, v_β) velocities only advect the water parcels in the front. The (u, v_1) components are responsible for vortex induction mechanisms on the front (PS86). Far from the coast, the jet does not “feel” the boundary and the undisturbed and beta components are zonal. The evolution of the jet is then governed by PS86’s infinite jet physics. Mathematically, this implies that as $r_- \rightarrow \infty$, $K_1(r_-) \rightarrow 0$, and the second integral on the right-hand side of [Eqs. \(16a\)](#) and [\(16b\)](#) becomes negligible. PS86 and [Pratt \(1988\)](#) have shown that advection and vortex induction generally oppose each other. This process is summarized in [Fig. 6](#)  . For example, the nonuniform eastward advection of the disturbance is illustrated in [Fig. 6a](#)  [the vortex-induction part of the model (u_1, v_1) is “turned off”]. Note the tendency for wave breaking on the west side of the bump. In [Fig. 6b](#)  , the westward Rossby-wave-like motion tendency, as a result of vortex induction mechanisms, is isolated. The combined advection and vortex induction in PS86’s balance may lead to meander detachment ([Fig. 6c](#) ) through simultaneous backward and forward wave breaking.

Near the coast, however, the balance is somewhat different from that of the infinite jet problem. For example, consider

the meridional boundary case where $\psi_0 + \beta\psi_\beta$ represents a steady state. If the contour is perturbed northward, as in the previous case, the southward-flowing coastal current will try to restore the contour toward the $y = 0$ latitude. On the other hand, the vortex induction mechanisms will cause both the vorticity wave motion and a dipole effect. The latter effect results in the interaction of a contour anomaly with its image due to the presence of the western boundary. In the case of an anticyclonic disturbance, the dipole effect will tend to cause the contour to move northward by pairing with its image (see [Fig. 7](#) ) .

The numerics of the contour dynamics algorithm described next follow PS86. The time-dependent position of the contour is determined by tagging parcels along the potential vorticity front and following their motion using Eq. (17). A second-order Runge–Kutta scheme is employed in the discretization of Eq. (17). At each time step, the three different contributions to the total velocities u and \mathbf{v} must then be determined. The undisturbed velocity is interpolated within grids previously obtained by the iterative scheme. The disturbed velocity is evaluated from Eq. (16), which has been discretized using a midpoint integration rule, according to Zou et al. (1987) and [Polvani \(1988\)](#). In order to maintain the model's resolution, a simple particle insertion–deletion scheme is applied to maintain the front particle separation at a preselected average distance, δ . The model accuracy is assessed using the conservation of area arguments presented by [Bell and Pratt \(1994\)](#). By delimiting a box defined between the coast and $x_e = 100$ and $y_e = -10$ and 10 , we estimate that the area underneath (beneath) the disturbed contour $\bar{y}(x) + \eta(x, t)$ increases (decreases) an average one thousandth of a percent per time step.

b. The asymmetric front model


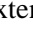
Now consider the asymmetric case, in which the potential vorticity in the lower half of the model ($q = -1 - \alpha$) and in the upper half ($q = 1 - \alpha$) can differ in magnitude. The range for the asymmetry parameter is $-1 < \alpha < 1$, where positive (negative) values correspond to a stronger current in the lower (upper) half of the domain. For this potential vorticity distribution, $\psi \rightarrow 1 + \alpha$ in the southern gyre and $\psi \rightarrow -1 + \alpha$ in the northern gyre. Since $\psi = 0$ at the western boundary, we see that the southern current transport is $1 + \alpha$, while the magnitude of the northern transport is $1 - \alpha$. Thus, α is half the difference in transports between the northern and southern boundary currents.

In contrast to the symmetric model, in which the undisturbed contour is a straight line connected to the coast and the center streamline in the zonal jet corresponds to $\psi_0 = 0$, the asymmetric model center jet streamline corresponds to $\psi_0 = \alpha$. This is easily seen by considering the inversion relationship for the meridional western boundary case [Eq. (6b)] in the far-field limit as $x \rightarrow \infty$ with asymmetric forcing:

$$\left(\frac{\partial^2}{\partial y^2} - 1\right)\psi_0 = \begin{cases} 1 - \alpha & \text{for } y > 0 \\ -1 - \alpha & \text{for } y < 0, \end{cases} \quad (18)$$

for which the solution is

$$\psi_0 = \alpha + \text{sgn}(-y)(1 - e^{-|y|}). \quad (19)$$

The evaluation of [Eq. \(19\)](#) at $y = 0$ yields the $\psi_0 = \alpha$ result. [Figure 4](#)  shows that all streamlines for the symmetric model, other than $\psi_0 = 0$, have hyperbolic shapes. We would not expect that the asymmetric model streamlines will differ much from this. Hence, if a steady asymmetric front exists, it would also have a hyperbolic-like shape, as do the streamlines in [Fig. 4](#) . Thus, it would not be connected to the coast, but rather extend southward paralleling the coast. The y contour should then approach the $\psi_0 = \alpha$ streamline as $x \rightarrow \infty$, and $y \rightarrow -\infty$ (for $\alpha > 0$) or $y \rightarrow \infty$ (for $\alpha < 0$). For example, consider the $\alpha > 0$ case, in which the $\psi_0 = \alpha$ streamline approaches a cross-shore distance of $x = x_0$ as $y \rightarrow -\infty$. The inversion relationship for the boundary current is

$$\left(\frac{\partial^2}{\partial x^2} - 1\right)\psi_0 = \begin{cases} -1 - \alpha & \text{for } x > x_0, \\ 1 - \alpha & \text{for } x < x_0. \end{cases} \quad (20)$$

Assuming $\psi_0 = 0$ at the coast, [Eq. \(20\)](#) has a solution of the form

$$\left[(-1 + \alpha) + be^{-x} + ce^x \text{ for } x < x_0,\right.$$

where the constants a , b , and c are

$$a = (1 - \alpha) - (e^{x_0} + e^{-x_0})$$

$$b = -\alpha + (1 - e^{-x_0})$$

$$c = e^{-x_0}$$

and x_0 is

$$x_0 = -\ln(1 - \alpha). \quad (22)$$

The corresponding “undisturbed” contour $\bar{y}(x, y)$ is then formally defined as the asymptotes of a hyperbolic streamline,

$$\bar{y}(x, y) = \begin{cases} y & \text{for } y < 0, x = x_0 \\ -(x - x_0) \tan\theta & \text{for } y \geq 0, x > x_0. \end{cases} \quad (23)$$

Analogous expressions can be derived for the case in which $\alpha < 0$.

The asymmetric model q and its components are sketched in [Fig. 8](#). The formalism of the asymmetric model is not presented here due to a more complicated form of the potential vorticity front as described by $\bar{y} = \bar{y}(x, y)$ and $\eta = \eta(x, y, t)$. It suffices to say that the asymmetric model is conceptually and numerically similar to the symmetric version (as a comparison between [Figs. 3](#) and [8](#) suggests). Actually, the symmetric model can be regarded as the asymmetric model in the limiting case of $x_0 \rightarrow 0$ or $\alpha \rightarrow 0$. The ψ_0 field is calculated by iteration. For example, the boundary conditions needed to determine ψ_0 for the $\alpha > 0$ case on the iterative scheme are

$$\begin{aligned} \psi_0 &= 0 \quad \text{at } x = 0 \\ &= (-1 + \alpha)(1 - e^{-x}) \quad \text{as } y \rightarrow \infty \\ &= (1 + \alpha) + ae^{-x} \quad \text{for } x > x_0, \quad \text{as } y \rightarrow -\infty \\ &= (-1 + \alpha) + be^{-x} + ce^x \quad \text{for } x < x_0, \\ &\quad \text{as } y \rightarrow -\infty \\ &= \alpha + \text{sgn}(-y)(1 - e^{|-y|}) \quad \text{as } x_e \rightarrow \infty. \end{aligned}$$

Notice that the last condition establishes that the zonal jet profile in the ocean interior for the asymmetric model is still the same as PS86's. The velocities associated with ψ_1 are computed by contour integrals identical to Eq. (16), and the ψ_β component is the same as in the symmetric case.

The cases of small and $O(1)$ α values will be explored considering the same θ values as in the symmetric model. [Figure 9](#) shows the ψ_0 fields for $\alpha = 0.65$ as an example. Notice that in contrast to the symmetric model, the asymmetric model has a northward (and stronger) boundary current velocity core, which is not located at the coast but is centered offshore at $x = x_0$. This is a consequence of the fact that asymmetry has introduced a potential vorticity band of different signs (between $x = 0$ and $x = x_0$) in the stronger current region. Physically, we believe that this opposite-sign nearshore q band can be interpreted as a result of (i) viscous effects due to the “rubbing” of the western boundary current against the boundary in the real ocean (as contour dynamics requires inviscid physics, the nearshore q band would to certain extent “mimic” the frictional effect on the asymmetric model q distribution) or (ii) the modification of the western boundary current in the real ocean by mixing with coastal waters (with distinct potential vorticity signatures). That the nearshore q band has exactly the same nominal value of the northern gyre q is a limitation of the single-front configuration. This constraint can be relaxed if a multifront model is considered.

However, the velocity core located at $x = x_0$ in the asymmetric model is certainly more realistic than the one corresponding to the symmetric model because friction inhibits the velocity near the wall in the real ocean. Therefore, the need for matching velocities across the nearshore q band and the $\psi = 0$ condition at the wall work to some degree as a nonstress boundary condition in our inviscid CD model.

This may help to explain why the flow structure in the asymmetric model resembles the one of the viscous, barotropic model by [Cessi \(1991\)](#). As in the present model, Cessi's was characterized by two asymmetric boundary currents that formed a separating zonal jet. Since the [Cessi \(1991\)](#) model included friction, no-slip conditions were used in the western boundary and the boundary current velocity cores were placed at some distance from the coast. In our inviscid model, we have free-slip boundary conditions and the coastal current maximum velocities occur at the q contour.

3. Numerical experiments

a. The symmetric model results

A series of numerical experiments were conducted with the symmetric model. In this subsection, we describe and discuss the results. [Table 2](#) defines the initial value problems performed.

1) THE MERIDIONAL BOUNDARY CASE

The known steady-state solution for the meridional boundary case, represented by $\psi_0 + \beta\psi_\beta$, is given in [section 2a](#). There, a qualitative description of how advection and vortex induction mechanisms may govern the contour motion close to the coast was presented. Here, some of PS86's experiments are repeated by perturbing the contour with isolated finite amplitude disturbances. The goal is to determine the effect of the boundary in the system dynamics. As in PS86's work, these disturbances are of the order of the deformation radius, in an attempt to make advection and vortex induction mechanisms of the same order.

To better understand vortex induction mechanisms as a combination of wave motion tendency and dipole effect, we "turn off" the shear flow in the model (i.e., ψ_0 is set to zero) and let $\beta = 0$. The contour is perturbed upward with a half Gaussian bump, which has the form

$$\eta(x, 0) = Ae^{-x^2}, \quad (24)$$

where $A = 0.5$. This disturbance represents an anticyclonic anomaly which has a velocity structure similar to that of the perturbed infinite jet problem on the east side (cf. [Fig. 10a](#) with [Fig. 6b](#)). The difference is, of course, the presence of the boundary on the west side. The no-normal-flow condition at the boundary [$u_1(0, t) = 0$] is created by pairing the anomaly with its image to the west of the boundary (or landward side of the model) as shown previously ([Fig. 7](#)). Thus the northward velocity u_1 is enhanced. As time progresses, the westward wave propagation tendency creates a westward velocity in the southeast corner of the anomaly. The velocity is large enough to cause wave breaking and sequential detachment of the anomaly from the zonal front ([Fig. 10b](#)). Meanwhile, in the northwest corner, the anomaly continues to be pushed northward. After separation the eddy continues to move northward ([Fig. 10c](#)).

We now solve the complete problem, in which the basic state is a shear flow with zero β ([Fig. 4a](#)), using the same initial condition as above (Run s1 in [Table 2](#)). [Figure 11](#) shows clearly that the advective effects of the southward coastal current overcome the dipole effect, and the anomaly is squashed against the x axis. Waves are generated at the ocean side of the bump. The waves travel eastward, with shorter wavelengths outrunning the large ones, resembling a spatially damped wave pattern. After some time ($t = 100$), the disturbance amplitude at the coast is approximately zero.

There are two ways to increase the relative effect of the vortex induction mechanisms (the dipole effect in particular) in the model: One is to increase the size of the disturbance in the initial conditions (PS86). The other is to include β , which in a piecewise constant potential vorticity field weakens the restoring capability of the ψ_0 field.

In Run s2, the size of the amplitude initial disturbance is set to four times that of Run s1; that is, $A = 2$ in [Eq. \(24\)](#) ([Fig. 12](#)). With much larger anomalous velocities (u_1, u_1), the Gaussian bump is squashed more slowly. At $t = 100$, the amplitude of the bump is about a quarter of its initial value. However, we do not observe any significant difference regarding between the wave pattern in this experiment and that in Run s1. Of course, the amplitudes are larger, but the waves have approximately the same wavelengths as the previous case. Note also that at $t = 10$ ([Fig. 12](#)), Runs s1 and s2 (in particular) resemble the model output when the basic shear is turned off ([Fig. 10](#), $t = 4$). However, in the presence of

basic shear, the eastward advection velocity u_0 overcomes the westward wave velocity u_1 in the trough to the east of the initial bump, so that no eddy detachment occurs. Given the symmetry between the upper and lower halves of the model, a cyclonic Gaussian bump (i.e., $A = -2$) yields a pattern like those of Runs s1 and s2 (see [Figs. 11](#) and [12](#)), with $\eta(x, t)$ being replaced by $-\eta(x, t)$.

In Run s3, the size of the initial disturbance in Run s1 is retained, but β is given a value of 0.1. This β is about five times the typical midlatitude value, but it is of the right order of magnitude for more tropical cases such as the North Brazil Current retroflexion around 7° – 8° N (Brown et al. 1992). As this case demonstrates, exaggerating β is analogous in some ways to the use of a larger initial disturbance (Run s2), because the beta velocity field opposes, and thus weakens, the undisturbed velocity field. As a consequence, the dipole effect is able to balance (at around $t = 10$) and eventually overcome the southward advection (see [Fig. 13](#)). In contrast to results of the previous experiment, we obtained a slowly (temporally) growing, spatially damped wave pattern that slowly propagates away from the coast within the time length of our run. The wavelengths in this case are somewhat shorter than the ones in the $\beta = 0$ cases.

In Run s4 (results not shown), we consider the same bump amplitude as in Run s2 and a smaller β value (0.05) than Run s3. The results are qualitatively identical to the Run s3 except that it has a higher growth rate due to a larger initial disturbance.

In Run s5, the effect of steepening the slope of the disturbance is investigated by starting with

$$\eta(x, 0) = 2\{1 - \tanh[10(x - 1)]\} \quad (25)$$

and $\beta = 0$. PS86 found this type of initial condition more efficient in causing eddies to detach in the infinite jet problem (as in [Fig. 6](#)). In our case, however, the results are very similar to those of Run s2 ([Fig. 12](#)) but with slightly larger wave amplitudes.

In an effort to pinch off an eddy, we used PS86's two-lobe initial disturbance (Run s5), given by

$$\eta(x, 0) = -A(x - d)e^{-(x-d)^2}, \quad (26)$$

where $A = 0.5$, $d = 0.5$. The calculations were initialized with a large positive potential vorticity anomaly to the east and a negative one near the coast. This represents an attempt to initially provide enough westward u_1 at the southeast corner of the anticyclonic bump to overcome the positive u_0 and to develop a pattern similar to the one depicted in [Fig. 10](#). However this initial condition failed to result in a detached eddy. Instead, it produces a pattern similar to that in Run s2 ([Fig. 12](#)) but with an enlarged trough to the east of the anticyclone at the coast. In a final case, with the same initial disturbance and $\beta = 0.1$ (Run s7, not shown), the model again fails to pinch off a coastal eddy.

The results from the previous experiments contrast with the infinite jet case where nonlinear effects are important. PS86 showed that, for an initial disturbance with dimensions of the deformation radius, the competition between advection and vortex induction could lead to meandering and eddy shedding ([Fig. 6](#)). In our case, the presence of the boundary imposes a different balance between the mechanisms, and hence the qualitatively different results are obtained here. For example, in Run s2 an amplitude disturbance as large as in PS86's experiments certainly creates disturbed velocities large enough to prevent the bump from being squashed quickly. However, since there is obviously no zonal advection at $x = 0$, there is no possibility of backward wave breaking (in a way similar to [Fig. 6a](#)). The dipole effect, which accounted for the eddy shedding on the "anomaly" model run, is opposed and overcome by the southward current advection. On the northeast side of the bump, the alongshore velocities associated with westward wave motion tendencies and advection have the same sign. As described above, no westward cross-shore velocity is created, making forward wave breaking unlikely. When β is included (Runs s3 and s4), the effects of the undisturbed velocity field are weakened by the beta and dipole effect velocity fields. On the eastward side of the disturbance, the westward beta velocity is not large enough to allow a pattern similar to the one in [Fig. 10b](#) to develop.

Our model results also show that perturbing the front at the coast excites fairly sinusoidal long waves. There is very little indication of nonlinear steepening, suggesting a predominantly linear behavior. A linearized version of the contour dynamics model is presented in the appendix and reproduces qualitatively the results obtained in this section.

The wave pattern obtained in this work resembles the ones obtained by [Pratt \(1988\)](#), which dealt with the long-wave limit of the PS86 model. The former author obtained the same fairly slowly dispersing wave pattern on an infinite domain, as found for initial disturbance amplitudes considered here. It should be emphasized that he explicitly filtered out short wavelengths, which our model does not. The presence of the western boundary and the zonal shear region it creates seems to somehow impose the long-wave approximation. To verify this finding, we use a simple linear calculation that considers an infinite jet similar to PS86's but with a linear zonal gradient in some region of the domain. The role of such structure is to

mimic the boundary effect. The center jet velocity is then given by

$$u(x, 0) = mx, (27)$$

where m is a constant coefficient.

The linearized PS86's potential vorticity front evolution equation is

$$\frac{\partial \eta}{\partial t} + \frac{\partial}{\partial x} [u\eta - \psi] = 0, (28)$$

where ψ satisfies

$$(\nabla^2 - 1)\psi = -2\delta(y)\eta(x, t). (29)$$

If we assume a solution for η of the form

$$\eta = Ae^{i[k(t)x - \int_0^t \omega(t') dt']}, (30)$$

use the Green's function method in [Eq. \(29\)](#) to solve for ψ , and apply [Eq. \(27\)](#), we obtain

$$x \left(\frac{\partial k}{\partial t} + mk \right) = \omega + im - \frac{k}{\sqrt{k^2 + 1}}. (31)$$

By collecting the $O(x)$ terms, we determine the wavenumber evolution

$$\frac{\partial k}{\partial t} = -mk, (32)$$

which has a solution of the form

$$k(t) = k_0 e^{-mt}, (33)$$

where k_0 is the dominant wavenumber in the initial disturbance. This result indicates that if the jet is perturbed in a region of the alongjet shear, the wave structure will have progressively smaller (larger) wavenumbers (wavelengths) no matter how large k_0 is. Therefore, the system will rapidly approach the long-wave limit in accordance with our model results.

We may again use linear theory to explain why the β -plane experiments yielded shorter waves than the f -plane results. The (nondimensional) linearized phase speed c expression (derived by PS86 for the infinite jet problem and modified to include β)

$$c = 1 - \frac{1}{(k^2 + 1)^{1/2}} - \beta (34)$$

is plotted in [Fig. 14](#) for $\beta = 0$ (solid curve) and $\beta = 0.1$ (dashed curve). Our model results indicate that the coastline causes the waves with phase speed close to zero to be favored. From [Fig. 14](#), we see that the slowest waves are shorter when β is nonzero.

2) THE TILTED BOUNDARY CASE

Now we consider the case in which the boundary is tilted. In contrast to the cases in the previous section where large input disturbances caused a momentum imbalance and a quasi-stationary wave pattern, here the tilt is responsible for the imbalance. The details of the momentum imbalance in the tilted boundary case are made explicit in the linear model formulation, which is presented and discussed in the appendix.

In Run s8, the case for $\beta = 0$ and a tilt of $\theta = \pi/4$ is considered first. The initial condition used simply corresponds to the shape of the $\psi_0 = 0$ streamline. [Figure 15](#) shows that, when the model is "turned on," a positive potential vorticity

anomaly develops close to the coast and a negative anomaly develops to the east side. Long waves are then excited (as in the cases of the previous section) and a spatially damped wave pattern results. However, in contrast to the $(\theta = 0, \beta = 0)$ cases, a slow linear temporal growth occurs.

Analogously to the meridional coast case, the results from the contour dynamics model do not differ qualitatively from the linear solution (see appendix) where a temporally growing, spatially damped long-wave pattern is also obtained. The average growth rates, given in terms of the time rate of change of latitude of a front particle at the coast, is -0.03 and may be regarded as the time variation in the separation latitude between the two current systems.

The next model experiment (Run s9) repeats Run s8 except with $\beta = 0.1$ (Fig. 16). The same wave pattern is obtained, but with a higher linear growth rate. As in the $\theta = 0$, nonzero β experiments, the waves excited are about 30%–40% shorter than the f -plane cases [see Eq. (34) and Fig. 14]. The amplitudes are about 20% higher.

A simple explanation for the growth rates in the long-wave amplitudes that may be given is to regard the steady momentum input as a forcing. Then, the linear growth would occur due to resonant nearly stationary waves (close to zero phase speed) being excited. The role of “forcing” of the coastline tilt becomes particularly clear when the contour evolution equation in the linear model [Eq. (A18) in the appendix] is examined. There, the coastline tilt effect explicitly acts as a steady forcing term and drives the slowly growing long waves in the linear experiments. We believe that this is a result of unbalanced alongshore momentum fluxes in the undisturbed velocity fields.

The southwestward migration of the separation latitude in unbalanced converging current systems was also obtained by [Agra and Nof's \(1993\)](#) model. These authors examined steady states for converging jets that were made possible by the steady migration of the whole current system.

Our results are also somewhat similar to those from the barotropic broad jet model by [Campos and Olson \(1991\)](#). Those authors studied quasi-stationary wave patterns on a spatially constant zonal mean flow, using a model which included a meridional western boundary and lateral Laplacian dissipation. Despite the different physics, they obtained temporally growing spatially damped wave patterns similar to our results. In that model, the frictional boundary works as a permanent sink of potential vorticity. In the inviscid model considered here, the tilt creates a source of potential vorticity which excites the near-stationary waves. Another interesting similarity between the two models is that larger β values were associated with shorter damped waves despite the different representations of the β effect.

b. The asymmetric model results

In this section, we will emphasize f plane asymmetric model experiments (Table 3). Examples of asymmetric currents on the β plane will be reported in section 4.

1) THE MERIDIONAL BOUNDARY CASE

In order to isolate the effect of asymmetry, we consider experiments with $\theta = 0$ and only positive α values, given the symmetry between the two halves of the model domain. All experiments used the shape of the streamline $\psi_0 = \alpha$ as initial conditions.

In the first experiment (Run a1), a very small asymmetry ($\alpha = 0.05$) is considered. This results in the northward current being about 10% more intense than the southward one (Fig. 17a). There is a striking similarity to the tilted boundary problem: slowly temporally growing, dispersing waves that resemble a damped wave pattern are generated. Similar patterns are obtained in the experiments with increasing asymmetry, corresponding to $\alpha = 0.22$ (Run a2, Fig. 17b) and 0.65 (Run a3, Fig. 17c), respectively.

In Fig. 18, we plot the latitude of the northernmost particle in the front for the three experiments at $t = 100$ (circles). We included the three corresponding $\alpha < 0$ cases, given

$$\begin{aligned} \bar{y}(x, y, -\alpha) + \eta(x, y, t, -\alpha) \\ = -[\bar{y}(x, y, \alpha) + \eta(x, y, t, \alpha)]. \end{aligned}$$

The zero α case corresponds to the symmetric model steady-state result.

It is seen in Fig. 18 that the asymmetry strengths and wave amplitudes vary linearly. The wavelengths excited are approximately the same in the three experiments. These results clearly indicate that the asymmetry in current transport plays a role similar to that of the coastline tilt. In other words, the asymmetry introduces a momentum imbalance in the alongshore

direction as in the symmetric, tilted model. This imbalance causes near-stationary waves to be excited as before. Therefore, it is possible to think of the asymmetry effect also as a forcing, related here to some sort of inertial overshoot.

[Agra and Nof \(1993\)](#) were able to find steady-state solutions for asymmetric, inviscid converging jets in the f plane. In their model, a static steady state was possible only when the converging currents had the same velocity at the coast. When the velocities were different, they found a steady migration of the stronger current system toward the weaker one. Unlike the model presented in this work, the departing jet veering angle is a result of their calculations. In ours, it is prescribed at infinity to make the jet zonal in the ocean interior. This assumption probably sustains the alongshore momentum imbalance that triggers the long waves.

[Cessi \(1991\)](#) found steady states in her viscous barotropic quasigeostrophic converging jet model. Retroreflection patterns were obtained, as in our results. In some of her experiments, a steady retroreflection eddy was formed at the western boundary. If the statement about the momentum imbalance in our model is correct, [Cessi's \(1991\)](#) result may be indicative that friction is needed to obtain steady states in an asymmetric converging jet system.

2) THE TILTED BOUNDARY CASE

In this series of experiments the coast is tilted in the presence of asymmetric coastal currents. In doing so, the symmetry in the geometry of the upper and lower halves of the model is lost and experiments with positive and negative α values are conducted.

The results from the two previous sections suggest that the forcing by the tilt and asymmetry will be additive when $\alpha > 0$ and will oppose each other for the $\alpha < 0$ cases.

The first pair of experiments employed a very small α , but with opposite signs. Run a4 ([Fig. 19a](#)) corresponds to $\alpha = 0.05$, and Run a5 ([Fig. 19b](#)) to $\alpha = -0.05$. As expected, the forcing by the tilt is much larger than the asymmetry effect and both results resemble the $\alpha = 0$ case ([Fig. 17](#)), with the waves having slightly higher (lower) amplitudes in the positive (negative) α values. Also, the wave pattern is evidently translated by a distance x_0 from the coast.

When we make $\alpha = \pm 0.22$ (Runs a6 and a7, [Figs. 19c and 19d](#)), about a third of the θ value, the forcing by asymmetry comes more effectively into play. The much smaller wave amplitudes and different pattern make evident the competition between the opposing forcing effects of tilt and asymmetry in [Fig. 19d](#), for which α is negative.

The asymmetry is of the same order as θ in Runs a8 and a9 ([Figs. 19e and 19f](#)), with $\alpha = \pm 0.65$. As expected, when the two $O(1)$ asymmetry and tilt effects add up, the highest amplitude waves among all f -plane experiments in this work are produced. On the other hand, when $\alpha < 0$, the asymmetry effect dominates and the wave amplitudes ([Fig. 19f](#)) resemble the ones obtained for the meridional boundary, small asymmetry case. The dominance of asymmetry in the balance is due the fact that the front is separated by about one deformation radius from the coast ($x_0 = 1.05$) and the effect of the tilted coastline decays eastward (see [Fig. A1](#) in the appendix). In other words, even with both effects having approximately the same strength, they are applied at different locations, and the front is closer to the influence of the asymmetry forcing.

From [Fig. 18](#) (circled curve) we could infer that there is possibly no steady state for an asymmetric converging current system (in our inviscid, equivalent-barotropic ocean on an f plane) when the western boundary is oriented meridionally. The results from [section 3a\(1\)](#) also suggest that there is no steady state for a symmetric converging current system when the coastline is slanted. However, when the tilt and asymmetry parameters have opposite signs (note that in [Fig. 18](#) the starred curve intersects the zero), the effects cancel each other, making a steady solution possible.

We chose to estimate the α value corresponding to the steady state for an asymmetric converging current system when the coastline is slanted by $\theta = \pi/4$ by employing the [Lebedev and Nof \(1996\)](#) momentum ratio formula:

$$\tan\theta = \left(\frac{m_{\text{south}} - m_{\text{north}}}{m_{\text{south}} + m_{\text{north}}} \right), \quad (35)$$

where

$$m_{\text{north}} = \int_0^{\infty} v^2|_{y \rightarrow \infty} dx \quad (36b)$$

are the momentum transport for southern and northern boundary currents, respectively. Lebedev and Nof's expression, in terms of the coastline angle, assures the momentum balance in our asymmetric current configuration. Using the ψ_0 definitions, $\theta = \pi/4$, and Eqs. (35)–(36), we obtain a value of $\alpha = -0.47$. In fact, we do find a numerical steady-state solution for the $\alpha = -0.47$ and $\theta = \pi/4$ values within our standard contour dynamics model resolution. The results of Run a10 are presented in Fig. 20.

4. Applications

In this section, we apply the model to three well-known western boundary current systems: the Gulf Stream, the Brazil Current, and the North Brazil Current. The variable scales and nondimensional parameters used in the three cases are presented in Table 4. The horizontal velocity scales U were estimated by matching the jet transport of our model with the observed transports.

a. The Gulf Stream

The Gulf Stream case is modeled as the convergence between the Gulf Stream and the slope water near Cape Hatteras to form the Gulf Stream extension. Schmitz and McCartney (1993) find that the transport in the upper kilometer of the Gulf Stream near Cape Hatteras, where it leaves the coast, to be about 55 Sv ($\text{Sv} \equiv 10^6 \text{ m}^3 \text{ s}^{-1}$) when it leaves the coast, and that the slope water transport is about 15 Sv. In terms of this model, the separating Gulf Stream is an asymmetric current system with $\alpha = 0.55$. Since α and θ have opposite signs, the effects oppose each other, with the asymmetry effect dominating. Consistent with PS86's scaling analysis, the β parameter is virtually negligible compared to the current vorticity gradient (about 1/60).

The results for the Gulf Stream run (Fig. 21a) reveal small amplitude, long meanders ($\approx 15 R_d$ or about 450 km). These wavelengths are similar to those seen in the mean satellite image composite of the north wall by Cornillon et al. (1986). The maximum meander amplitude occurs at a distance of $10 R_d$ from the coast, and for $t = 100$ it is about $0.35 R_d$ or 10.5 km. Using the position of the northernmost particle in the front, we can estimate the speed at which the largest lobe is moving eastward. Dimensionally, the main lobe "phase speed" is 8.7 km d^{-1} . This value compares reasonably well with the measurements of Tracey and Watts (1986), who found phase speeds of about 14 km d^{-1} for the wavelength range of 450–500 km close to Cape Hatteras.

It is not a surprise that an equivalent-barotropic, single-front model does not agree with many aspects of the observed configuration of the Gulf Stream extension with its growing meanders and ring production. Using a two-layer version of the PS86 jet model, Meacham (1991) showed that baroclinic instability can produce large amplitude meanders and eddy shedding of similar character to the ones observed for the Gulf Stream extension. A barotropically unstable version of the PS86 model, presented by Pratt et al. (1991), also produced eddies that resembled the warm outbreak events in the Gulf Stream. However, our model lacks baroclinic and barotropic instability mechanisms. The incorporation of baroclinic instability mechanisms into a version of the present model is in progress.

b. The Brazil–Malvinas confluence

The Brazil Current separates from the continental margin at approximately 38°S where its warm subtropical waters meet the cold subantarctic waters of the Malvinas Current to form the Brazil Current extension and later the South Atlantic Current (Olson et al. 1988; Stramma and Peterson 1990). According to Gordon and Greengrove (1986), Brazil Current geostrophic transport in the upper 1000 m is about 20 Sv and twice the transport for the Malvinas Current. Therefore, a Brazil Current experiment, analogous to the Brazil–Malvinas confluence (in the Northern Hemisphere, for convenience) with $\alpha = 0.33$, was conducted.


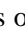
In contrast to the Gulf Stream situation, θ and α have the same sign in this case and therefore reinforce each other. Given the much less intense flow of the Brazil Current, its β scale is twice the value of its Northern Hemisphere counterpart.

The results for the Brazil Current run (Fig. 21b) are similar to the wavelength of about 450 km (at $t \approx 100$) found for the larger lobes of the previous f -plane experiments (β is small). As the South American coast is less deviated from a north–south orientation, $|\theta|$ is smaller than for the Gulf Stream case. Thus, the maximum amplitude value of about $1.9 R_d$ (or 57 km at $t = 100$) lies in between the two curves of Fig. 18.

The width of the larger lobes is in agreement with the 500 km found in [Olson et al.'s \(1988\)](#) analysis of satellite images. However, the amplitudes are reduced by a factor of 5. The large amplitude meanders and coastal eddy shedding observed by [Gordon and Greengrove \(1986\)](#) and [Olson et al. \(1988\)](#) can be attributed to barotropic or baroclinic instabilities. Numerical experiments with the Miami model by [Campos and Olson \(1991\)](#) indicated that barotropic instability caused meandering growth and eddy shedding in their simulations of the Brazil–Malvinas confluence.

c. The North Brazil Current

We now model the separation of the near-equatorial North Brazil Current as the convergence of its 45 Sv with a broader and slower southward branch of the North Equatorial Current, carrying about 35 Sv ([Johns et al. 1990](#); F. L. Bub 1996, personal communication). The convergence forms the western part of the North Equatorial Countercurrent. Since the separation occurs at about 7°N, the deformation radius is about four times larger than those for the midlatitude examples. Also, the nondimensional Rossby parameter β is 0.35, one order of magnitude higher than the previous examples.

The results for the North Brazil Current run ([Fig. 21c](#) ) show that the retroflexion is reproduced and that the wavelengths present at $t = 40$ are about 700–900 km. These values are consistent with [Richardson and Reverdin \(1987\)](#) and [Richardson et al. \(1994\)](#). The larger value of β causes the contour to be pushed against the boundary, and the main lobe grows northward (in a mechanism similar to the one described in Run s3). We acknowledge that the way the β effect is modeled here is somewhat arbitrary, since one could move the $\Psi_{\beta} = 0$ streamline north or south. However, the results in [Fig. 21c](#)  show striking resemblance to the maps of the North Brazil Current retroflexion in charts derived from satellite images presented by [Johns et al. \(1990\)](#) and surface drifter tracks by [Richardson et al. \(1994\)](#). In particular, the stretching of the retroflexion bulge prior to shedding an eddy has been observed. Unfortunately, this model does not result in the complete eddy detachment. Instead, it shows a slow linear stretch of the retroflexion bulge northwestward.

In contrast to the previous current system examples, there is no evidence in the literature that either baroclinic or barotropic instabilities may play a role in the North Brazil Current eddy shedding. It appears the processes governing the detachment in this case are yet to be uncovered.


5. Summary and conclusions

In this paper we have explored the effect of coastline orientation and transport asymmetry in converging western boundary currents that form a zonal eastward inertial jet. A single-vorticity-front contour dynamics model based on PS86's infinite jet model is developed to explore this system. The β effect is introduced in the model in such a way that the contour dynamics technique requirement of a piecewise constant potential vorticity field is satisfied. The β term is compensated for by including a time-independent flow field similar to the edge between two Fofonoff gyres. The parameter space of the model is spanned, including the coastline tilt angle θ , the transport asymmetry α , and the nondimensional Rossby parameter β .

For the case of a north–south coastline orientation ($\theta = 0$) and symmetric converging currents ($\alpha = 0$) that form a zonal jet, a steady state is known to exist. The PS86 experiments with isolated disturbances are repeated and the effect of the boundary is investigated. It is found that in the presence of the boundary, long waves are often excited and very little nonlinear steepening occurs as the flow evolves. The input of large potential vorticity anomalies leads to a slowly temporally decaying (growing) damped long-wave pattern in our f -plane (β -plane) calculations within the time length of our runs. This pattern resembles the quasi-stationary wave motion observed in western boundary current extensions. Relatively shorter waves occurred in the β -plane experiments. Coastal eddy detachment in these cases appears unlikely, even if fairly extreme boundary conditions are used. These results differ from the infinite jet experiments of PS86, where eddy shedding became possible when the same initial conditions were used. The presence of the western boundary—through the zonal gradient in the undisturbed cross-shore velocity component, required to satisfy the zero normal flow condition at the coast—causes a stretching of the disturbances so that the long-wave limit is reached rapidly and prevents wave breaking on the west side of the anomaly.

When either a nonmeridional coastline or converging current asymmetry are considered, a steady state is not obtained numerically. The tilt in coastline orientation ($\theta \neq 0$) imposes a momentum imbalance that creates a steady source of potential vorticity at the coastward end of the departing jet. This source drives temporally growing, spatially damped long waves. The linear slow growth observed in the wave pattern is probably associated with the steady input of alongshore momentum in the model. If the tilt effect is thought of as a steady forcing, as the linear model in the appendix suggests, the quasi-stationary long waves excited are close to the resonance (zero) frequency and may account for the slow linear growth of the amplitudes. Similar responses can occur when there is asymmetry in the coastal current transports, without coastline tilt.

For the cases in which we allow both θ and α to be nonzero, the dynamical effects of asymmetry and tilt can reinforce or oppose each other. When the coastline is tilted westward relative to the stronger current direction, they reinforce each other,

generating the retroflection type of separation (Fig. 1b ). When the coastline tilt is eastward, following the stronger current, the two effects oppose each other, accounting for much smoother separations. These results agree with [Ou and De Ruijter's \(1986\)](#) model results and [Campos and Olson's \(1991\)](#) description of boundary current separations. Steady-state solutions may be obtained for the latter case by means of total cancellation between tilt and asymmetry forcings.

The application of the model to three different separate boundary current systems qualitatively reproduces the separation patterns, and the observed wavelengths are within the observed range.

We acknowledge that the model is unbalanced in all unsteady runs described above. However, we believe that the model has shown that an inertial system can reproduce the patterns observed in separating boundary currents by introducing a momentum imbalance locally (i.e., close to the coast) through tilting the coastline or making the current system asymmetric. The downstream condition of constraining the jet to be zonal is also in agreement with observations of most boundary current extension flow patterns. In the real ocean, we expect that other forces (such as pressure forces and friction) would balance the system as whole, and a steady-state retroflection pattern may be possible.

Also, as one anonymous reviewer pointed out, from the works of Moore and Niiler (1974) and [Cushman-Roisin et al. \(1993\)](#), steady states for separating (symmetric and asymmetric) jets are possible on the β plane, while our results seems to suggest otherwise. Those authors found solutions consisting of spatially uniform, long stationary meanders in the ocean interior (the free jet region). Within the length of our runs, we found no indication that our β -plane experiments approach a steady state. We are, however, bounded by computational constraints. The Lagrangian nature of the contour dynamics code makes extremely long runs unviable, and we can only speculate about such disagreement. The path equation method by Moore and Niiler (1974) assumes that downstream variations are slow compared to cross-stream ones, and that, clearly, does not hold at the coast. There could be steady meanders in the far downstream free jet. S. P. Meacham (1996, personal communication) has found full steadily propagating $1\frac{1}{2}$ -layer states using contour dynamics and iteration. His results perhaps indicate that steady states can be found if the parameters and initial conditions are just right. All we can say from our results is that starting from a flat downstream state does not lead to a steady state within reasonable lengths of time.

In preparation is a version of the present model that incorporates baroclinic instability mechanisms by considering a $2\frac{1}{2}$ -layer configuration.

Acknowledgments

The authors wish to thank Lawrence J. Pratt (WHOI) for the rich and insightful discussions of this manuscript that helped to improve its content. We also thank Frank L. Bub (OPAL/UNH) for sharing his then new results on the North Brazil Current retroflection region, Frank O. Smith Jr. (OPAL/UNH) for his editorial assistance, and the two anonymous *JPO* reviewers. Ilson da Silveira's time was sponsored by the Conselho Nacional de Desenvolvimento Científico e Tecnológico (CNPq, Brasília, Brazil) under Grant 203112/90-3. Wendell Brown's time was funded by NSF under OCE-8912260. Glenn Flierl's time was funded by NSF under Grant OCE 93-14140.

REFERENCES

- Agra, C., and D. Nof, 1993: Collision and separation of boundary currents. *Deep-Sea Res. I*, **40**, 2259–2282..
- Bell, G. I., and L. J. Pratt, 1994: Eddy–jet interaction theorems of piecewise constant potential vorticity flows. *Dyn. Atmos. Oceans*, **20**, 285–314..
- Brown, W. S., W. E. Johns, K. D. Leaman, J. P. McCreary, R. L. Molinari, P. L. Richardson, and C. Rooth, 1992: A Western Tropical Atlantic Experiment (WESTRAX). *Oceanography* **5**, (1) 73–77..
- Campos, E. J. D., and D. B. Olson, 1991: Stationary Rossby waves in western boundary current extensions. *J. Phys. Oceanogr.*, **21**, 1202–1224.. [Find this article online](#)
- Cessi, P., 1991: Laminar separation of colliding western boundary currents. *J. Mar. Res.*, **49**, 697–717..
- Cornillon, P., 1986: The effect of the New England seamounts on the Gulf Stream meandering as observed from satellite IR imagery. *J. Phys. Oceanogr.*, **16**, 386–389.. [Find this article online](#)
- Cushman-Roisin, B., L. J. Pratt, and E. Ralph, 1993: A general theory for equivalent barotropic thin jets. *J. Phys. Oceanogr.*, **23**, 91–103.. [Find this article online](#)
- Gordon, A. L., and C. L. Greengrove, 1986: Geostrophic circulation of the Brazil–Falkland confluence. *Deep-Sea Res. I*, **33**, 573–585..

- Hall, M. M., and N. P. Fofonoff, 1993: Downstream development of the Gulf Stream from 68° to 55° W. *J. Phys. Oceanogr.*, **23**, 225–249.. [Find this article online](#)
- Houry, S., E. Dombrowsky, P. De Mey, and J. F. Minster, 1987: Brunt–Väisälä frequency and Rossby radii in the South Atlantic. *J. Phys. Oceanogr.*, **17**, 1619–1626.. [Find this article online](#)
- Johns, W. E., T. N. Lee, F. Schott, R. Zantopp, and R. H. Evans, 1990: The North Brazil Current retroflection: Seasonal structure and eddy variability. *J. Geophys. Res.*, **95**, 22 103–22 120..
- Lebedev, I., and D. Nof, 1996: The drifting confluence zone. *J. Phys. Oceanogr.*, **26**, 2429–2448.. [Find this article online](#)
- Meacham, S. P., 1991: Meander evolution on piecewise-uniform, quasi-geostrophic jets. *J. Phys. Oceanogr.*, **21**, 1139–1170.. [Find this article online](#)
- Moore, D. W., and P. P. Niiler, 1974: A two-layer model for the separation of inertial boundary currents. *J. Mar. Res.*, **32**, 457–484..
- Olson, D., G. Podesta, R. Evans, and O. Brown, 1988: Temporal variations in the separation of Brazil and Malvinas currents. *Deep-Sea Res. I*, **35**, 1971–1980..
- Ou, H. W., and W. P. M. De Ruijter, 1986: Separation of an inertial boundary current from a curved coastline. *J. Phys. Oceanogr.*, **16**, 280–289.. [Find this article online](#)
- Polvani, L. M., 1988: Geostrophic vortex dynamics. PhD thesis, MIT/WHOI Joint Program, WHOI-88-48, 221 pp..
- , N. J. Zabusky, and G. R. Flierl, 1989: Two-layer geostrophic vortex dynamics, Part 1: Upper-layer V-states and merger. *J. Fluid Mech.*, **205**, 215–242..
- Pratt, L. J., 1988: Meandering and eddy detachment according to a simple (looking) path equation. *J. Phys. Oceanogr.*, **18**, 1627–1640.. [Find this article online](#)
- , and M. E. Stern, 1986: Dynamics of potential vorticity fronts and eddy detachment. *J. Phys. Oceanogr.*, **16**, 1101–1120.. [Find this article online](#)
- , J. Earles, P. Cornillon, and J. F. Cayula, 1991: The nonlinear behavior of varicose disturbances in a simple model of the Gulf Stream. *Deep-Sea Res. I*, **38**, S591–S622..
- Pullin, D. J., 1992: Contour dynamics method. *Annu. Rev. Fluid Mech.*, **24**, 89–115..
- Richardson, P. L., and G. Reverdin, 1987: Seasonal cycle of the velocity in the Atlantic North Equatorial Countercurrent as measured by surface drifters, current meters, and ship drifts. *J. Geophys. Res.*, **92**, 3691–3708..
- , G. E. Hufford, R. Limeburner, and W. S. Brown, 1994: North Brazil Current retroflection eddies. *J. Geophys. Res.*, **99**, 5081–5093..
- Schmitz, W. J., and M. S. McCartney, 1993: On the North Atlantic circulation. *Rev. Geophys.*, **31**, 29–49..
- Stern, M. E., and L. J. Pratt, 1985: Dynamics of vorticity fronts. *J. Fluid Mech.*, **161**, 513–532..
- , and G. R. Flierl, 1987: On the interaction of a vortex with a shear flow. *J. Geophys. Res.*, **92**, 10 733–10 744..
- Stramma, L., and R. G. Peterson, 1990: The South Atlantic current. *J. Phys. Oceanogr.*, **20**, 846–859.. [Find this article online](#)
- Tracey, K. L., and D. R. Watts, 1986: On the Gulf Stream characteristics near Cape Hatteras. *J. Geophys. Res.*, **91**, 7587–7602..
- Wang, X., 1992: Interaction of an eddy with a continental slope. Ph.D. thesis, MIT/WHOI Joint Program, WHOI-92-40, 216 pp..
- Zou, Q., E. A. Overman, H. M. Wu, and N. J. Zabusky, 1988: Contour dynamics for the Euler equations: Curvature controlled initial node displacement and accuracy. *J. Comput. Phys.*, **78**, 350–372..

APPENDIX

6. The Linear Symmetric Model

a. The model formulation

The contour dynamics model developed in [section 2a](#) allows the nonlinear investigation for any coastline tilt [the angle θ may be $O(1)$]. Here, we consider the linearized case in which the coast orientation is either meridional or only slightly tilted from the north–south direction, that is, $\theta \ll 1$.

For easier manipulation of the equations, we first define a nonorthogonal coordinate system (x, ξ) , where x is still the cross-shore direction and ξ is the cross-front direction defined by

$$\xi = y - \bar{y}(x) \quad (\text{A1})$$

or, using [Eq. \(4\)](#),

$$\xi = y + x \tan\theta. \quad (\text{A2})$$

In terms of the new coordinate system, [Eq. \(3\)](#) becomes

$$\left[\frac{\partial^2}{\partial x^2} + 2 \tan\theta \frac{\partial^2}{\partial x \partial \xi} + (1 + \tan^2\theta) \frac{\partial^2}{\partial \xi^2} - 1 \right] \psi + \beta \xi \cos\theta = -1 + 2\mathcal{H}(\xi - \hat{\eta}), \quad (\text{A3})$$

where the carets denote the fields for the linearized model.

[Equation \(17b\)](#) is also rewritten, with \hat{v} as the new cross-front velocity:

$$\frac{d}{dt} \hat{\eta} = \frac{\partial \hat{\eta}}{\partial t} - \frac{\partial \psi}{\partial \xi} \frac{\partial \hat{\eta}}{\partial x} = \hat{v}(x, \hat{\eta}, t). \quad (\text{A4})$$

Under the $\theta \ll 1$ assumption, [Eq. \(A2\)](#) can be rewritten as

$$\xi = y - \theta x + O(\theta^2) \quad (\text{A5})$$

and $\hat{\psi}$ can be expanded in the asymptotic series

$$\hat{\psi} = \hat{\psi}_0 + \theta \hat{\psi}_1 + O(\theta^2). \quad (\text{A6})$$

In the linear regime, $\hat{\eta}$ is $O(\theta)$ so that

$$\mathcal{H}(\xi - \hat{\eta}) = \mathcal{H}(\xi) - \delta(\xi) \hat{\eta} + O(\hat{\eta}^2).$$

We can substitute [Eqs. \(A5\)](#) and [\(A6\)](#) into [Eqs. \(A3\)](#) and [\(A4\)](#) and collect the lowest terms to obtain

$$\left[\frac{\partial^2}{\partial x^2} + \frac{\partial^2}{\partial \xi^2} - 1 \right] \psi_0 + \beta \xi = -1 + 2\mathcal{H}(\xi) \quad (\text{A7})$$

and

$$\psi_0(x, 0) = 0, \quad (\text{A8})$$

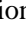
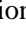
respectively. No restriction was imposed on the size of β to allow the model to be applied for conditions where $\beta > \theta$.

The $\hat{\psi}_0$ field is partitioned into “undisturbed” $\hat{\psi}_{00}$ and “beta” $\hat{\psi}_{0\beta}$ parts that satisfy

$$\left[\frac{\partial^2}{\partial x^2} + \frac{\partial^2}{\partial \xi^2} - 1 \right] \psi_{00} = -1 + 2\mathcal{H}(\xi) \quad (\text{A9})$$

and

$$\left[\frac{\partial^2}{\partial x^2} + \frac{\partial^2}{\partial \xi^2} - 1 \right] \psi_{0\beta} = -\xi, \quad (\text{A10})$$

respectively. Note that if we replace y with ξ and consider $\theta = \bar{y} = 0$, [Eqs. \(A9\)](#) and [\(A10\)](#) are of the same form as [Eqs. \(6\)](#) and [\(7\)](#). So are the boundary conditions and the solutions. Therefore, the solutions in [Figs. \(4a\)](#)  and [\(5a\)](#)  also respectively represent the solutions for $\hat{\psi}_{00}$ and $\hat{\psi}_{0\beta}$ in the (x, ξ) space.

Defining

$$\hat{u}_0 = -\frac{\partial \psi_0}{\partial \xi}, \quad (\text{A11})$$

the $O(\theta)$ equations are

$$\left[\frac{\partial^2}{\partial x^2} + \frac{\partial^2}{\partial \xi^2} - 1 \right] \psi_1 - 2\frac{\partial \hat{u}_0}{\partial x} = -2\delta(\xi)\hat{\eta} \quad (\text{A12})$$

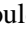

and

$$\frac{\partial \hat{\eta}}{\partial t} + \frac{\partial}{\partial x}(\hat{u}_0 \hat{\eta}) = \frac{\partial \psi_1}{\partial x} \quad (\text{A13})$$

evaluated at $\xi = 0$. We can also split the $\hat{\psi}_1$ field into $\hat{\psi}_{11}$ and $\hat{\psi}_{12}$, which satisfy

$$\left[\frac{\partial^2}{\partial x^2} + \frac{\partial^2}{\partial \xi^2} - 1 \right] \psi_{11} = 2\frac{\partial \hat{u}_0}{\partial x} \quad (\text{A14})$$

$$\left[\frac{\partial^2}{\partial x^2} + \frac{\partial^2}{\partial \xi^2} - 1 \right] \psi_{12} = -2\delta(\xi)\hat{\eta}, \quad (\text{A15})$$

respectively. It can be seen in the equations above that all time dependence of $\hat{\psi}_1$ is contained in its $\hat{\psi}_{12}$ component through $\hat{\eta}(x, t)$. Hence the time-independent $\hat{\psi}_{11}$ is determined by iteration. The required boundary conditions for [Eq. \(A14\)](#) can be determined by considering the $\beta = 0$ case, in which the x -dependence of \hat{u}_0 is confined to small values of x and ξ (see [Fig. 4a](#) ). Thus it is reasonable to assume that $\hat{\psi}_{11}$ should also decay as $x \rightarrow \infty$ and $\xi \rightarrow \pm\infty$. The solution for $\hat{\psi}_{11}$ is shown in [Fig. A1](#) .

The $\hat{\psi}_{12}$ field is obtained in terms of Green's functions G_+ and G_- , as defined in [Eq. \(12\)](#), and written in the (x, ξ) space according to

$$(A16)$$

By applying the δ -function properties to [Eq. \(A16\)](#) and evaluating it at $\xi = 0$,




$$\psi_{12} = \frac{1}{\pi} \int_0^{\infty} dx' [K_0(|x - x'|) - K_0(|x + x'|)] \hat{\eta}(x', t). \quad (A17)$$

The contour evolution [Eq. \(A13\)](#) for the linear model can be written in terms of $\hat{\psi}_{11}$ and $\hat{\psi}_{12}$,

$$\frac{\partial \hat{\eta}}{\partial t} + \frac{\partial}{\partial x} [\hat{u}_0 \hat{\eta} - \psi_{12}] = \frac{\partial \psi_{11}}{\partial x} \quad (A18)$$

or using [Eq. \(A16\)](#) to get

$$\begin{aligned} \frac{\partial \hat{\eta}}{\partial t} + \frac{\partial}{\partial x} \left\{ \hat{u}_0 \hat{\eta} - \frac{1}{\pi} \int_0^{\infty} dx' \right. \\ \left. \times [K_0(|x - x'|) - K_0(|x + x'|)] \hat{\eta}(x', t) \right\} \\ = \frac{\partial \psi_{11}}{\partial x}. \end{aligned} \quad (A19)$$

[Equation \(A18\)](#) [or [Eq. \(A19\)](#)] is a first-order wave equation for $\hat{\eta}$, which is steadily forced by $\hat{v}_{11}(0)$ ([Fig. A1](#) ). For the cases in which the coast is tilted, $\hat{\psi}_{11}$ exists and the time-independent part of streamfunction field does not coincide with the contour. Thus the quantities in the linear model $\hat{\psi}_0 + \theta \hat{\psi}_{11}$, where $\hat{\psi}_{11}$ accounts for the mismatch between the contour and streamline (as seen in [Figs. 4b](#)  and [5b](#) ) can be related to the corresponding quantities in the nonlinear model: the $\psi_0 + \beta \psi_\beta$ field.

Prior to the discretization of [Eq. \(A18\)](#), the integrals in [Eq. \(A17\)](#), as in [Eq. \(15\)](#), need to have the logarithmic singularity removed. Here, the desingularization is done in a slightly different manner from the method employed on the contour dynamics scheme. We follow the PS86 method here.

As an example, consider the first integral of the right-hand side of [Eq. \(A17\)](#). In the $|x - x'| \lesssim \epsilon$ interval where $\epsilon \ll 1$, the integral is singular. Hence, we can split the integral into nonsingular and singular parts, as follows:

$$\begin{aligned} \int_0^{\infty} dx' K_0(|x - x'|) \hat{\eta}(x', t) \\ = \int_{|x-x'| > \epsilon} dx' K_0(|x - x'|) \hat{\eta}(x', t) \\ + \int_{x-\epsilon}^{x+\epsilon} dx' K_0(|x - x'|) \hat{\eta}(x', t). \end{aligned} \quad (A20)$$

Note that the singularity is now confined to the second integral on the right-hand side.

Using the $\epsilon \ll 1$ assumption, we can approximate $\hat{\eta}(x', t)$ in the singular integral of [Eq. \(A20\)](#) by

$$\hat{\eta}(x', t) = \hat{\eta}(x, t) + O(\epsilon), \quad (\text{A21})$$

which yields

$$\begin{aligned} & \int_{x-\epsilon}^{x+\epsilon} dx' K_0(|x - x'|) \hat{\eta}(x', t) \\ &= -\hat{\eta}(x, t) \int_{x-\epsilon}^{x+\epsilon} dx' \ln(|x - x'|) + O(\epsilon), \quad (\text{A22}) \end{aligned}$$

given that $K_0(r) = -\ln(r) + O(\epsilon)$ for $r \leq \epsilon$.

The integral on the right-hand side of [Eq. \(A22\)](#) can be easily integrated by parts to obtain

$$\int_{x-\epsilon}^{x+\epsilon} dx' \ln(|x - x'|) = -2\epsilon[\ln(\epsilon) - 1] + O(\epsilon), \quad (\text{A23})$$

With [Eqs. \(A22\)](#) and [\(A23\)](#) in [Eq. \(A20\)](#), we get

$$\begin{aligned} & \int_0^{\infty} dx' K_0(|x - x'|) \hat{\eta}(x', t) \\ &= \int_{|x-x'| > \epsilon} dx' K_0(|x - x'|) \hat{\eta}(x', t) \\ & \quad - 2\epsilon[\ln(\epsilon) - 1] \hat{\eta}(x, t) + O(\epsilon). \quad (\text{A24}) \end{aligned}$$

A similar procedure should be applied to the second integral on the right-hand side of [Eq. \(A17\)](#).

Having desingularized the integrals in the $\hat{\psi}_{12}$ expression, we can discretize [Eq. \(A18\)](#). The numerical procedure used in this model is based on an Eulerian scheme, unlike the Lagrangian contour dynamics algorithm. Therefore, values for $\hat{\eta}(x, t)$ will be evaluated on a grid of fixed “ x ” values. Hence, considering

$$x_{(i)} = i\Delta x \quad \text{for } i = 0, M \quad (\text{A25a})$$

$$t^{(n)} = n\Delta t \quad \text{for } n = 0, N, \quad (\text{A25b})$$

we use a modified Lax finite difference scheme to approximate [Eq. \(A18\)](#) as

$$\frac{\Delta x}{\Delta x} = \frac{\Delta x}{\Delta x}, \quad (\text{A26})$$

which is solved together with

$$\begin{aligned} \psi_{12(i)}^{(n)} = \frac{\Delta x}{\pi} & \left[\sum_{j \neq i} K_0(|x_{(i)} - x_{(j)}|) \hat{\eta}_{(j)}^{(n)} - \left(\ln \frac{\Delta x}{2} - 1 \right) \hat{\eta}_{(i)}^{(n)} \right. \\ & - \sum_{j \neq 0} K_0(|x_{(i)} + x_{(j)}|) \hat{\eta}_{(j)}^{(n)} \\ & \left. + \left(\ln \frac{\Delta x}{2} - 1 \right) \hat{\eta}_{(i)}^{(n)} \delta(j) \right], \end{aligned} \quad (\text{A27})$$

where

$$\delta(j) = \begin{cases} 1 & \text{for } j = 0 \\ 0, & \text{otherwise} \end{cases}$$

and ϵ was taken to be equal to $\Delta x/2$.

For the beginning of the domain ($i = 0$), we simply use

$$\begin{aligned} & \frac{\hat{\eta}_{(0)}^{(n+1)} - \hat{\eta}_{(0)}^{(n)}}{\Delta t} + \frac{\hat{u}_{0(1)} \hat{\eta}_{(1)}^{(n)} - \hat{u}_{0(0)} \hat{\eta}_{(0)}^{(n)}}{\Delta x} - \frac{\psi_{12(1)}^{(n)} - \psi_{12(0)}^{(n)}}{\Delta x} \\ & = \frac{\psi_{11(1)} - \psi_{11(0)}}{\Delta x}. \end{aligned} \quad (\text{A28})$$


The far-end boundary condition is obtained by choosing an M large enough to guarantee that $\hat{\eta}_{(M)}^{(n+1)} = 0$.



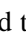
The numerical stability criteria is given by

$$\left| \frac{\Delta t}{\Delta x} \hat{u}_{0\text{MAX}} \right| \leq 1. \quad (\text{A29})$$

b. Numerical results

In this section we repeat some of the initial value problems described in [section 3a](#) using the linear physics.

The meridional boundary case. For the $\theta = 0$ case, $\bar{y}(x)$ and $\hat{\psi}_{11}$ are also zero, and [Eq. \(A18\)](#) becomes homogeneous. We then perform the Run 11 experiment, which is the linear analog of Run s2. In [Fig. A2a](#) , it can be verified that the same wave pattern as in the nonlinear model is obtained. The waves have approximately the same wavelengths, but the apparent spatial “damping” seem stronger.

The tilted boundary case. By including a slight tilt in the coastline, for example, $\theta = \pi/40$, the linear model also repeats the behavior of its contour dynamics counterpart. Run 12 ([Fig. A2b](#) ) and Run 13 ([Fig. A2c](#) ) represent the linear analogs of the Run s8 and Run s9 respectively. The steady input of alongshore momentum is made explicit by the \hat{v}_{11} velocity. Even though we just show the final time step of both model runs in [Fig. A2](#) , it is verified that the growth rate in the wave pattern is similar to the nonlinear calculations.

Tables

Table 1. The model variable scales.

Definition	Convention
Horizontal length scale (=Rossby radius of deformation)	R_d
Horizontal velocity (= f -plane center jet velocity)	U
Timescale	$R_d U^{-1}$
Potential vorticity	$U R_d^{-1}$
Rosby parameter	$U R_d^{-2}$

[Click on thumbnail for full-sized image.](#)

Table 2. Summary of numerical experiments with the symmetric model.

Run	θ	β	Initial conditions
s1	0	0	Eq. (24), $A = 0.5$
s2	0	0	Eq. (24), $A = 2.0$
s3	0	0.1	Eq. (24), $A = 0.5$
s4	0	0.05	Eq. (24), $A = 2.0$
s5	0	0	Eq. (25)
s6	0	0	Eq. (26), $A = 2, d = 1.5$
s7	0	0.1	Eq. (26), $A = 2, d = 1.5$
s8	$\pi/4$	0	$\psi_0 = 0$ streamline shape
s9	$\pi/4$	0.1	$\psi_0 = 0$ streamline shape

[Click on thumbnail for full-sized image.](#)

Table 3. Summary of numerical experiments with the asymmetric model.

Run	θ	α	Initial conditions
a1	0	0.05	$\psi_0 = \alpha$ streamline shape
a2	0	0.22	$\psi_0 = \alpha$ streamline shape
a3	0	0.65	$\psi_0 = \alpha$ streamline shape
a4	$\pi/4$	0.05	$\psi_0 = \alpha$ streamline shape
a5	$\pi/4$	-0.05	$\psi_0 = -\alpha$ streamline shape
a6	$\pi/4$	0.22	$\psi_0 = \alpha$ streamline shape
a7	$\pi/4$	-0.22	$\psi_0 = -\alpha$ streamline shape
a8	$\pi/4$	0.65	$\psi_0 = \alpha$ streamline shape
a9	$\pi/4$	-0.65	$\psi_0 = -\alpha$ streamline shape
a10	$\pi/4$	-0.47	$\psi_0 = -\alpha$ streamline shape

[Click on thumbnail for full-sized image.](#)

Table 4. Scales and nondimensional parameters for the three study cases.

Current system	Length/ scale		θ	α	β
	(km)	U (m s^{-1})			
Gulf Stream	30 ^a	1.2 ^b	$-\pi/4$	0.55 ^c	0.014
Brazil Current	30 ^d	0.5 ^e	$\pi/6$	0.33 ^f	0.033
North Brazil Current	110 ^g	0.8 ^h	$\pi/4$	0.03 ⁱ	0.348

^a Calculated by G. R. Flierl as R_d using a section of the SYNOP dataset from Hall and Fofonoff (1993).

^b Estimated from Schmitz and McCartney (1993).

^c Estimated from Schmitz and McCartney (1993).

^d Estimated as R_d from Houry et al. (1987).

^e Estimated from Gordon and Greengrove (1986).

^f Estimated from Gordon and Greengrove (1986).

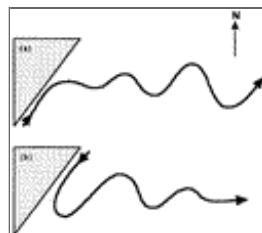
^g Estimated as R_d from Houry et al. (1987).

^h Estimated from transport calculations using the Western Tropical Atlantic Experiment dataset (E. L. Bub 1996, personal communication).

ⁱ E. L. Bub (1996, personal communication).

[Click on thumbnail for full-sized image.](#)

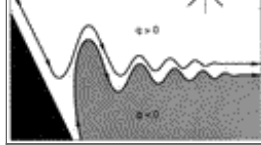
Figures



[Click on thumbnail for full-sized image.](#)

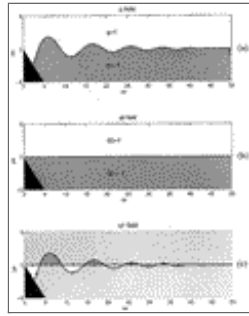
Fig. 1. Schematic separation of western boundary currents: (a) the Gulf Stream and (b) the Brazil Current.





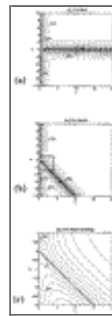
[Click on thumbnail for full-sized image.](#)

Fig. 2. The model geometry. The model coordinate system is rotated by an angle θ relative to the earth Cartesian coordinates (x_e, y_e) .



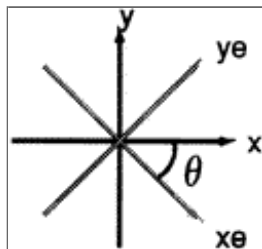
[Click on thumbnail for full-sized image.](#)

Fig. 3. (a) The total potential vorticity field q for the symmetric model is composed of (b) q_0 , the part of the field associated with the undisturbed (or straight) position $\bar{y}(x)$ of the front, and (c) q_1 , part of the field associated with the deviations from the undisturbed field q_0 . The arrows indicate the integration direction.



[Click on thumbnail for full-sized image.](#)

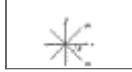
Fig. 4. The undisturbed streamfunction ψ_0 solution for the symmetric model, in which (a) $\theta = 0$, (b) $\theta = \pi/4$, and (c) $\theta = \pi/4$ as a closeup of the region around the origin. Results are expressed in the model coordinates (x, y) . The potential vorticity discontinuity is represented by a solid line, and the streamlines by dashed lines.



[Click on thumbnail for full-sized image.](#)

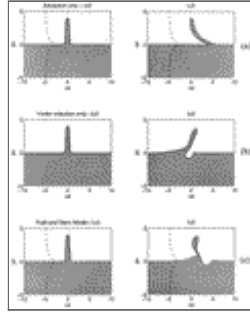
Fig. 4. The undisturbed streamfunction ψ_0 solution for the symmetric model, in which (a) $\theta = 0$, (b) $\theta = \pi/4$, and (c) $\theta = \pi/4$ as a closeup of the region around the origin. Results are expressed in the model coordinates (x, y) . The potential vorticity discontinuity is represented by a solid line, and the streamlines by dashed lines.





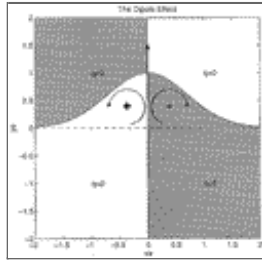
Click on thumbnail for full-sized image.

Fig. 5. The results for the β -related streamfunction Ψ_β for (a) $\theta = 0$ and (b) $\theta = \pi/4$. Results expressed in the model coordinates (x, y) .



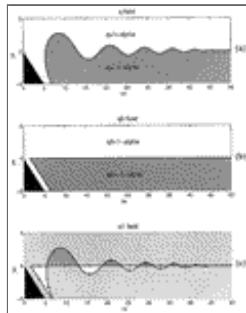
Click on thumbnail for full-sized image.

Fig. 6. Physical processes involved in the evolution of a potential vorticity front: (a) advection of a passive front by the background shear flow; (b) vortex induction mechanisms where the basic shear flow has been turned off; and (c) the [Pratt and Stern \(1986\)](#) balance, which is a superposition of the effects in (a) and (b). The basic jet profile is represented by the dashed line.



Click on thumbnail for full-sized image.

Fig. 7. The dipole effect associated with the presence of a boundary in an anticyclonic anomaly. In an inviscid system, the zero normal flow condition at the boundary is satisfied by pairing the vortex with its image. The net result is the movement of an anticyclonic anomaly along the boundary, toward larger y values. The net motion is in the opposite direction for a cyclonic anomaly.



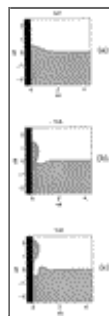
Click on thumbnail for full-sized image.

Fig. 8. (a) The total potential vorticity field q for the asymmetric model comprises (b) q_0 , the part of the field associated with the undisturbed position $\bar{y}(x)$ of the front, and (c) q_1 , the part of the field associated with the deviations from the undisturbed field q_0 field. The arrows indicate the integration direction.



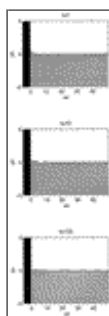
[Click on thumbnail for full-sized image.](#)

Fig. 9. The undisturbed streamfunction ψ_0 solution for the asymmetric model ($\alpha = 0.65$) in which (a) $\theta = 0$ and (b) $\theta = \pi/4$. Results are expressed in the model coordinates (x, y). The potential vorticity discontinuity is represented by a solid line, and the streamlines by dashed lines.



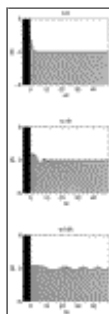
[Click on thumbnail for full-sized image.](#)

Fig. 10. The anomaly model experiment, in which only vortex mechanisms are present for (a) $t = 0$, (b) $t = 4$, and (c) $t = 8$.



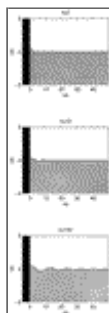
[Click on thumbnail for full-sized image.](#)

Fig. 11. Symmetric model experiment with $\theta = 0$ and $\beta = 0$. Initial conditions are given by [Eq. \(24\)](#) in main text, with a disturbance amplitude of $A = 0.5$ (Run s1). The y -axis scale is amplified about four times relative to the x -axis scale.



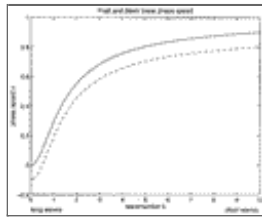
[Click on thumbnail for full-sized image.](#)

Fig. 12. Same as [Fig. 11](#) but using a disturbance amplitude of $A = 2$ (Run s2). The y -axis scale is amplified about four times relative to the x -axis scale.



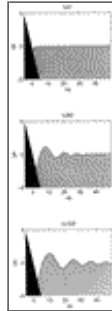
[Click on thumbnail for full-sized image.](#)

Fig. 13. Same as [Fig. 12](#) but using $\beta = 0.1$ (Run s3). The y -axis scale is amplified about four times relative to the x -axis scale.



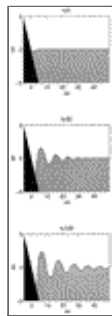
Click on thumbnail for full-sized image.

Fig. 14. Linearized phase speed for [Pratt and Stern's \(1986\)](#) infinite jet using $\beta = 0$ (solid curve) and $\beta = 0.1$ (dashed curve).



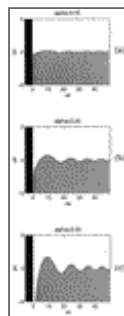
Click on thumbnail for full-sized image.

Fig. 15. Symmetric model experiment with $\theta = \pi/4$, $\beta = 0$ (Run s8). Initial conditions are given by the shape of the streamline $\psi_0 = 0$. The y-axis scale is amplified about four times relative to the x-axis scale.



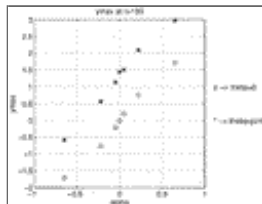
Click on thumbnail for full-sized image.

Fig. 16. Same as [Fig. 15](#) but using $\beta = 0.1$ (Run s9). The y-axis scale is amplified about four times relative to the x-axis scale.



Click on thumbnail for full-sized image.

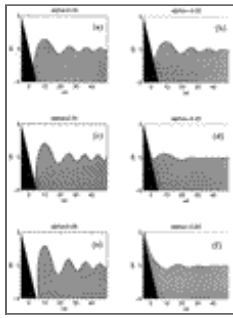
Fig. 17. Asymmetric model experiment results with $\theta = 0$, $\beta = 0$ at $t = 100$ for (a) $\alpha = 0.05$ (Run a1), (b) $\alpha = 0.22$ (Run a2), and (c) $\alpha = 0.65$ (Run a3). The y-axis scale is amplified about four times relative to the x-axis scale.



Click on thumbnail for full-sized image.

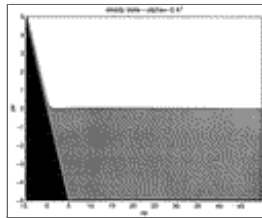
Fig. 18. Position of the northernmost particle in the front at $t = 100$ as a function of the asymmetry parameter α for $\theta = 0$ (circled

curve) and $\theta = \pi/4$ (starred curve); β is zero for all the simulations.



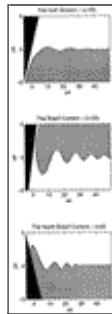
[Click on thumbnail for full-sized image.](#)

Fig. 19. Asymmetric model experiment results with $\theta = \pi/4, \beta = 0$ at $t = 100$ for (a) $\alpha = 0.05$ (Run a4), (b) $\alpha = -0.05$ (Run a5), (c) $\alpha = 0.22$ (Run a6), (d) $\alpha = -0.22$ (Run a7), (e) $\alpha = 0.65$ (Run a8), and (f) $\alpha = -0.65$ (Run a9). The y-axis scale is amplified about four times relative to the x-axis scale.



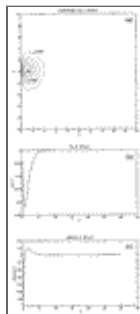
[Click on thumbnail for full-sized image.](#)

Fig. 20. The steady state obtained for asymmetric model experiment Run a10 with $\theta = \pi/4, \beta = 0$, and $\alpha = -0.47$. The y-axis scale is amplified about four times relative to the x-axis scale.



[Click on thumbnail for full-sized image.](#)

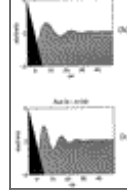
Fig. 21. The boundary current applications: (a) the Gulf Stream case at $t = 100$ ($\theta = \pi/4, \beta = 0.014, \alpha = -0.55$); (b) the Brazil–Malvinas confluence case at $t = 100$ ($\theta = \pi/6, \beta = 0.033, \alpha = 0.33$); and (c) the North Brazil Current case at $t = 40$ ($\theta = \pi/4, \beta = 0.348, \alpha = 0.3$).



[Click on thumbnail for full-sized image.](#)

Fig. A1. The “mismatch” streamfunction ψ_{11} in the (x, ξ) space: (a) in the model domain, (b) along $\xi = 0$, and (c) its zonal gradient along $\xi = 0$.





Click on thumbnail for full-sized image.

Fig. A2. Linear symmetric model experiment results at $t = 100$ for (a) $\theta = 0, \beta = 0$ (Run 11), (b) $\theta = \pi/40, \beta = 0$ (Run 12), and (c) $\theta = \pi/40, \beta = 0.1$ (Run 13). The y -axis scale is amplified about four times relative to the x -axis scale.

* Current affiliation: Department de Oceanografia Física, Instituto Oceanográfico, Universidade de São Paulo, São Paulo, Brazil.

Corresponding author address: Dr. Glenn R. Flierl, Department of Earth, Atmospheric and Planetary Sciences, MIT, Room 54-1426, Cambridge, MA 02139.

E-mail: glenn@lake.mit.edu

top ▲



© 2008 American Meteorological Society [Privacy Policy and Disclaimer](#)
Headquarters: 45 Beacon Street Boston, MA 02108-3693
DC Office: 1120 G Street, NW, Suite 800 Washington DC, 20005-3826
amsinfo@ametsoc.org Phone: 617-227-2425 Fax: 617-742-8718
[Allen Press, Inc.](#) assists in the online publication of AMS journals.